Nanoscale Advances

ROYAL SOCIETY OF CHEMISTRY

PAPER

View Article Online
View Journal | View Issue

Cite this: *Nanoscale Adv.*, 2025, **7**, 2599

Chiral induction in the crystallization of KIO_3 and $LiIO_3$: the role of amino acids in controlling the chirality of inorganic crystals†

Matan Oliel * and Yitzhak Mastai

Received 3rd December 2024
Accepted 27th February 2025

DOI: 10.1039/d4na01006j

rsc.li/nanoscale-advances

Chiral induction in crystals has attracted significant attention due to its implications for developing chiral materials and understanding mechanisms of symmetry-breaking enantioselective crystallization of naturally occurring chiral minerals. Despite its potential use in chiral discrimination, this area remains largely unexplored. Here, we investigate chiral induction during crystallization of naturally occurring chiral KIO_3 and $LiIO_3$ minerals using arginine and alanine as chiral inducers. The chiral nature of the crystallization and the effect of the chiral inducers were examined using circular dichroism, polarimetry, and low-frequency Raman spectroscopy. The impact of chiral molecules on the rate and final crystal structure was studied by electron microscopy including SEM and TEM. We demonstrate that it is possible to control the chirality with chiral exogenous molecules, mainly amino acids. Understanding chiral induction in crystal growth may open avenues for controlled assembly of chiral materials and development of novel functional materials with unique properties.

Introduction

Chirality is often associated with organic molecules; however, many inorganic compounds also exhibit chirality in their crystal structures. This chirality in inorganic crystals generally results from a chiral arrangement of non-centrosymmetric metal chelates or oxides. For instance, quartz (SiO_2) demonstrates chirality in its α polymorph due to the chiral arrangement of SiO_2 units.

Studies on the chirality of chiral inorganic crystals are surprisingly limited.[1] The surface of chiral inorganic crystals holds significant promise for various applications including chiral discrimination,[2–5] chiral sensing[6] and enantioselective catalysis.[7,8] Understanding how surface chirality is influenced by chiral induction and controlling chirality in these materials is crucial, as chiral selectivity occurs primarily on the material surface.[9]

In recent years, chirality has been found to play an important role in nanotechnology.[10–12] Chirality plays a useful role in many nano-systems, such as chiroptical molecular switches,[13–15] molecular motors, chiral nanosurfaces[16–26] and chiral nanoparticles.[27–39] Overall, the areas of chiral nanoscience and nanotechnology show exceptional promise for further developments in areas such as catalysts, bio-recognition and chiral separation processes.[40]

One good example of chiral surfaces is chiral selectivity on metal surfaces that are well-established, in particular with cubic closed-packed (CCP) metals.[41] Crystal planes such as Cu (6,4,3) and Au (3,2,1) exhibit chiral properties despite the lack of chirality of bulk metals. These surface features yield exceptional enantiomeric excess (e.e) during adsorption of small chiral molecules.[4,42]

In recent decades, remarkable strides have been made in exploring the nature of inorganic chiral surfaces and systems. Pioneering research led by the Gellman group unveiled the chirality of high-Miller-index planes in metallic surfaces, revealing their enantiospecific adsorption in the presence of chiral molecular probes.[6,17] Research led by Hazen and collaborators emphasized the significance of chiral inorganic crystal surfaces, in particular in mineral-catalyzed organic synthesis and the interactions between biomolecules and mineral surfaces.[1,43,44] In a series of publications, Hazen *et al.* carefully documented numerous common rock-forming minerals, predominantly chiral oxides and silicates, which exhibit chiral crystal surfaces, showcasing the chiral selection of amino acids on these surfaces.[45,46]

However, naturally occurring chiral minerals including quartz (SiO_2),[47] monohydrocalcite ($CaCO_3 \cdot H_2O$),[48] wulfingite (ε-$Zn(OH)_2$)[49] and α-HgS[50,51] have received little attention. Some chiral minerals are believed to contribute to the development of homochirality in biological molecules through an extensive process of chiral discrimination.[52,53] Studying the influence of chiral amino acids on the formation of chiral minerals and

Department of Chemistry, Institute for Nanotechnology and Advanced Materials, Bar-Ilan University, Ramat-Gan 5290002, Israel. E-mail: Yitzhak.Mastai@biu.ac.il; matanoliel5@gmail.com

† Electronic supplementary information (ESI) available: Materials, and FTIR spectra of L/D-Arg-induced KIO_3 and L/D-Ala-induced $LiIO_3$ crystals. See DOI: https://doi.org/10.1039/d4na01006j

replicating the natural conditions in which this occurs provides valuable insights into these processes. This research can also elucidate mechanisms that control chiral biomolecules. While some chiral minerals form the chiral phase in a straightforward manner, the crystallization of certain chiral crystals is more complex. For example, berlinite, the quartz-like chiral form of $AlPO_4$, requires high annealing temperatures to transform into its chiral phase.[54,55] These extreme conditions present challenges for analysis of chiral induction.

To address this issue, we sought chiral inorganic systems that crystallize under relatively simple conditions, mainly at low temperature and in aqueous solutions. Potassium iodate (KIO_3)[56,57] and lithium iodate ($LiIO_3$)[58,59] are perfect examples. KIO_3 and $LiIO_3$ are naturally occurring chiral minerals with space groups of $P1$ and $P6_322$, respectively, which are easy to crystallize, and their chiral phases are stable at room temperature (RT). As water-soluble salts, their chirality and chiral induction have apparently not been investigated.

Here, we present our research on the control of chirality of KIO_3 and $LiIO_3$ crystals by chiral induction with amino acids. The crystal morphology and structural changes were confirmed by X-ray diffraction (XRD), Fourier transform infrared (FTIR) spectroscopy and high-resolution scanning electron microscopy (HR-SEM). Moreover, the chirality was analyzed by circular dichroism (CD) spectroscopy of crystal pellets and using an optical polarizer for low-frequency Raman (LFR). The enantioselectivity and chiral discrimination were proved by CD and polarimetry by performing chiral adsorption experiments.

Experimental methods

Materials

The materials used in this research are detailed in the ESI (S1).†

Preparation of chiral-induced crystals

Chiral-induced KIO_3 crystals were synthesized by recrystallization using a slow cooling method. Supersaturated solutions in double distilled water (DDW) were prepared, heated to 50 °C and stirred until complete dissolution. After dissolution, 10% (moles/to KIO_3 moles) of L/D-Arg were added and the solution was stirred for 15 min and spontaneously cooled to RT by turning off the hot plate and keeping the solution on it to allow as slow a cooling process as possible and then the solution was refrigerated overnight. The white crystals were filtered in a vacuum, washed several times with ethanol to remove Arg traces and dried at RT.

The chiral-induced $LiIO_3$ crystals were synthesized by a slow evaporation method using the following reaction:

$$Li_2CO_3 + 2HIO_3 \rightarrow 2LiIO_3 + H_2O + CO_2$$

In a typical case, 0.5 g of lithium carbonate (Li_2CO_3) and 2.375 g of iodic acid (HIO_3) were dissolved in 20 mL of DDW. The solutions were put in an oil bath and heated to 60 °C under stirring at pH 10 to allow the reaction to occur. The basic conditions were achieved by adding lithium hydroxide (LiOH). After dissolution, 60.6 mg of L/D-Ala (10% moles of Li_2CO_3) were added and the solution was covered by pierced aluminum foil to prevent contamination and allow evaporation. The stirring was stopped after 24 h and the heating was maintained at 60 °C in the oil bath to maintain constant temperature until complete evaporation. To remove residual Ala, clear white crystals were soaked for 24 hours in 9 : 1 MeOH/DDW in a glass beaker. The cleaned crystals were filtered and dried in an oven at 50 °C.

Characterization methods

The crystallographic structures of KIO_3 and $LiIO_3$ were determined by XRD using a Bruker AXS D8 Advance diffractometer with Cu Kα ($\lambda = 1.5418$ Å) operating at 40 kV/40 mA, in the range from 10 to 80°.

FTIR was performed using a Thermo Scientific Nicolet iS10 spectrometer equipped with a Smart iTR attenuated total reflectance sampler with a single bounce diamond crystal. Data were collected in the 530–4000 cm^{-1} range at a spectral resolution of 4 cm^{-1} and analyzed using OMNIC software.

HR-SEM images were taken using a field-emission FEI (Helios 600) instrument. Samples were sputtered with gold.

KIO_3 and $LiIO_3$ crystals' chirality measurements

Pellets (KBr, 300 mg, 5/10% L/D-induced Li/KIO_3) were prepared (mixed and pressed under 10 ton for 3 min) and measured by CD in a designated holder at different orientations at RT with a Chirascan spectrometer (Applied Photophysics, UK).

LFR was carried out on an inVia Raman microscope (Renishaw, UK) at RT under an optical microscope with a 50× objective. The samples were excited using a 514 nm laser source with a P-polarization (vertical) ratio of 100 : 1 (0.5 mW, 40 s) and spectra were acquired using a polarizer with 1800 L mm^{-1} grating in the range of 100–1500 cm^{-1}.

Chiral adsorption onto KIO_3 and $LiIO_3$ crystals

Tartaric acid (TA) was chosen due to its solubility in ethanol in which KIO_3 and $LiIO_3$ are insoluble. Chiral adsorption measurements were carried out with CD by preparing a 2.5 mM solution of D/L-TA or DL-TA in ethanol and adding L-Arg-induced KIO_3 crystals or L/D-Ala-induced $LiIO_3$ crystals in several concentrations. The crystals were kept suspended in solution overnight using a rotary suspension mixer and filtered out using a 0.2 mm filter. The filtered solutions were taken for CD measurement and compared to pure D/L-TA or DL-TA solutions.

Chiral adsorption using a polarimeter was performed by preparing a 5 wt% solution of D/L-TA in ethanol and adding L-Arg-induced KIO_3 or L-Ala-induced $LiIO_3$ crystals in several concentrations. The crystals were kept suspended in solution overnight using a rotary suspension mixer and filtered out using a 0.2 mm filter. The filtered solutions were taken for polarimeter measurement and compared to pure D/L-TA solutions. The solutions were measured at RT using a Jasco P-2000 polarimeter.

The selectivity was calculated by measuring the polarization ratio of the enantiomer (adsorption peak maxima) with respect to the pure enantiomer.

For the selectivity, measurement by mass change was carried out by preparing a 20 mM of D/L-TA solution in ethanol and adding D-Ala-induced $LiIO_3$ at a concentration of 32 mg mL^{-1}. The crystals were kept suspended in solution overnight using a rotary suspension mixer and filtered out using a 0.2 mm filter. The filtered solutions were evaporated and the mass change calculated and compared to the mass of D/L-TA before the adsorption.

Results and discussion

Characterization

First, we studied the changes in the structure and morphology by XRD and FTIR following chiral induction using amino acids. In all samples, the main crystalline structure of KIO_3 at RT was the stable triclinic phase with chiral space group $P1$ (COD ID: 4318187) and the main diffraction peak at $2\theta = 28.2°$ corresponding to its (2, −2, 2) plane (Fig. 1I). The cell units a, b, and c are 8.923, 8.942, and 7.709 Å, respectively, and α, β, and γ are 54.4, 125.3, and 90.6°, respectively. The unchanged diffractions indicate that the crystalline structure is maintained. $LiIO_3$ displays a crystalline structure that fits the RT stable hexagonal phase with chiral space group $P6_322$ (COD ID: 1529711). The key diffraction peak at 25.5° corresponds to the (1, 0, 1) plane (Fig. 1II). The unit cell dimensions were $a = 5.478$ Å, $b = 5.478$ Å, and $c = 5.17$ Å with $\alpha = \beta = 90°$ and $\gamma = 120°$. Similar to KIO_3, the consistent results indicate that the structure was maintained.

We also characterized the crystals by FTIR to check for structural changes or traces of amino acid. Both pristine and chiral-induced KIO_3 showed the same spectra and indicated two peaks, close to each other, with a broad peak at 722 cm^{-1} and a very small peak at 797 cm^{-1}. Both peaks represent the vibration modes of the oxygen–iodine bonds (Fig. S2I†). Similarly, the $LiIO_3$ crystals showed two peaks belonging to the O–I vibration modes and no difference between the pristine and chiral-induced crystals (Fig. S2II†). However, we noticed a redshift at 763 and 860 cm^{-1} probably due to the effect of the cation on the vibration mode energies in the lattice. Moreover, the control $LiIO_3$ sample also has a broad absorbance peak between 1400, and 1700 cm^{-1} associated with C=O indicating some unreacted Li_2CO_3.

Morphology and surface analysis

The morphology was examined by HR-SEM. The control KIO_3 crystals exhibit a square shape and smooth surface (Fig. 2I and IV); however, with the amino acid the morphology and surface change. The L-Arg-induced KIO_3 crystals maintain a square shape albeit with a rough surface (Fig. 2II and V), while the D-Arg-induced KIO_3 crystals are hexagonal with a smooth surface similar to the control (Fig. 2III and VI).

Fig. 3 presents HR-SEM images of $LiIO_3$ crystals. Pristine $LiIO_3$ shows an uneven morphology and very rough surface (I and IV). In contrast, L-Ala-induced $LiIO_3$ crystals have a more hexagonal shape with a smoother surface (II and V). D-Ala-

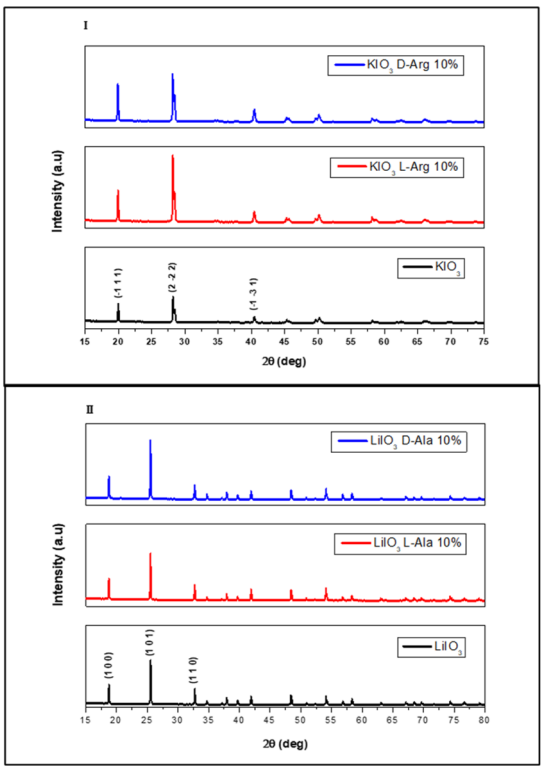

Fig. 1 XRD of KIO_3 (I) and $LiIO_3$ crystals (II) – control (black), L-Arg-induced (red) and D-Arg-induced (blue) displaying the main diffraction planes of triclinic KIO_3 and hexagonal $LiIO_3$.

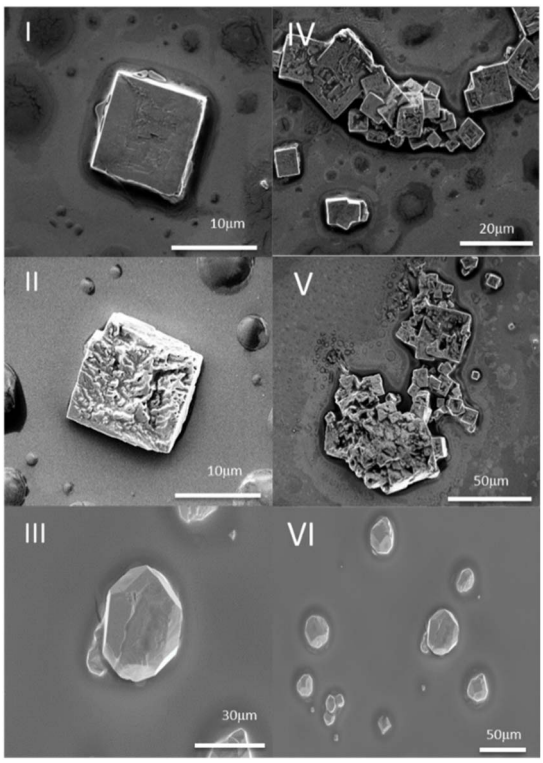

Fig. 2 HR-SEM images of KIO_3 crystals – control (I, IV/10, 20 μm), L-Arg-induced KIO_3 (II, V/10, 50 μm) and D-Arg-induced KIO_3 (III, VI/30, 50 μm).

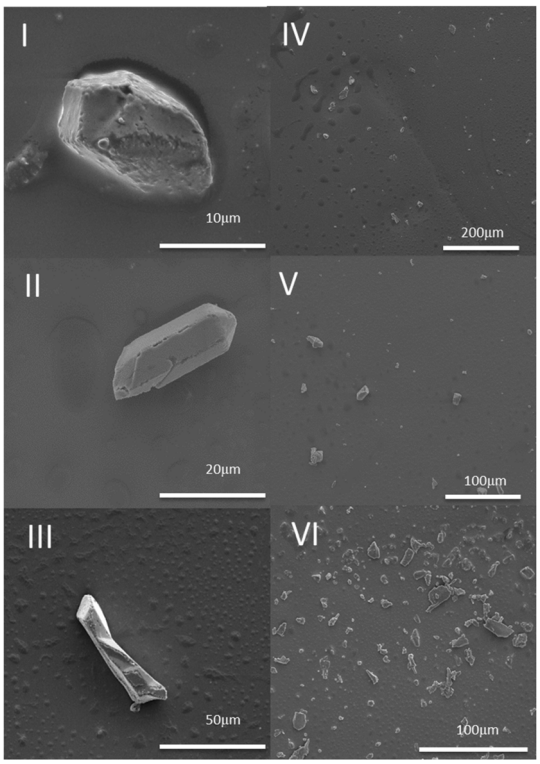

Fig. 3 HR-SEM images of $LiIO_3$ crystals – control (I, IV/10, 200 μm), L-Ala-induced $LiIO_3$ (II, V/20, 100 μm) and D-Ala-induced $LiIO_3$ (III, VI/50, 100 μm).

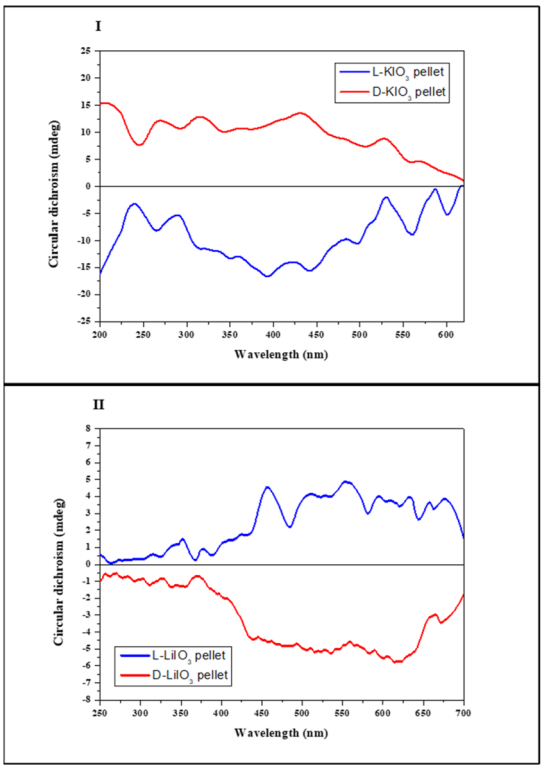

Fig. 4 CD spectra of L/D-Arg-induced KIO_3 (I) and L/D-Ala-induced $LiIO_3$ (II) pellets.

induced $LiIO_3$ crystals have an uneven morphology similar to pristine $LiIO_3$ with a rougher surface, which is smoother than the surface of pristine $LiIO_3$ (III and VI).

Direct chirality measurements

To prove the chiral preference, we measured the crystals with CD and LFR. For CD measurement, L/D-Arg-induced KIO_3 and L/D-Ala-induced $LiIO_3$ pellets were prepared and measured at different angles. The CD measurement of the chiral-induced KIO_3 crystals shows two chiral signal areas: a wide one from 525 to 275 nm, and a narrow one below 525 nm.

Moreover, a positive signal is seen for the D-Arg-induced crystals and a negative one (anticlockwise direction polarization) for L-Arg-induced KIO_3 (Fig. 4I). In contrast, LiO_3 (Fig. 4II) presents opposite signals – positive for L-Ala-induced $LiIO_3$ and negative for D-Ala-induced $LiIO_3$. $LiIO_3$ crystals also display a wide chiral signal from 600 to 400 nm. Both CD spectra show the optical activity of the iodate crystals proving their chiral preference.

While this measure does not provide absolute chirality, the relative purity can be obtained by the most frequent polarizations. The polarization of L-Ala-induced $LiIO_3$ is +4 mdeg *vs.* −6 mdeg for D-Ala-induced $LiIO_3$, thus the latter crystals are 1.5 times purer. L-Arg-induced KIO_3 is 1.2 times purer than the D-Arg-induced crystals (−15/+12.5 mdeg for L/D-Arg-induced KIO_3).

The chirality was also measured by low frequency Raman spectroscopy (LFR),[60] a new technique that allows direct measurement of the chirality employing the low-frequency region of the spectrum, which highlights lattice-level interactions and global molecular fluctuations. These lower frequencies are associated with vibrations from weaker bonds and long-range interactions making them highly sensitive to changes in polarization. The enantiomers were excited using fixed polarized light and collected using a movable optical polarizer. The polarized light can be horizontal (S-Pol) or vertical (P-Sol). One enantiomer gives a stronger signal for S-Pol, while the other gives a stronger signal for P-Pol.

Aviv *et al.* presented a method that differentiates racemic and enantiopure crystals of amino acids. Intensity changes and wavenumber shifts were seen in single crystals of arginine, aspartic acid and valine.[61] Nematsov *et al.* used LFR to analyze the chiral purity of crystals and showed specific vibrational mode changes as a function of the enantiomeric purity.[62] Moreover, they investigated the dependence of the signal intensity on the orientation of L-Ala single crystals showing correlation between signal intensities with the proximity between the incident beam direction and the orientations of the intermolecular interactions.[63] This makes LFR a powerful method to prove chiral preference by direct measurement.

As iodate salts, the Raman spectra of KIO_3 and $LiIO_3$ are quite similar (Fig. S3†) and can be divided into three areas: 700–800 cm^{-1} (iodate vibrational modes), 300–400 cm^{-1} (free translational motion of the iodate anion) and 100–200 cm^{-1} (lattice vibrational modes).

We used the LFR method to examine the effect of KIO_3 and $LiIO_3$ chiral-induced crystals on the collection of light through

a polarizer at different angles (S-Pol and P-Pol), where the enantiomers of the crystal under test are supposed to give opposite effects to each other in intensities at same angles. Moreover, in order to prove the effect precisely, the comparison is of the angles for each crystal separately when the light is collected from the same point in the sample in order to neutralize as many factors as possible that could affect the measurements.

Fig. 5I presents the LFR of chiral-induced crystals. Higher intensity is evident for the L-Ala-induced KIO_3 crystals when the light is collected at P-Pol with the maximum intensity ratio P-Pol/S-Pol of 1.225 at 303 cm^{-1}. In contrast, D-Ala-induced $LiIO_3$ crystals produce higher intensity when the light is collected at S-Pol with the maximum S-Pol/P-Pol intensity ratio at 329 cm^{-1} of 1.247 (Fig. 5II).

The LFR results support previous measurements. Iodate crystals with higher P-Pol intensity are more prone to be L type, while those with higher S-Pol intensity tend to be D type crystals. Similar results were obtained for D-Arg-induced KIO_3 and L-Ala-induced $LiIO_3$ (Fig. S4†). LFR signifies long-range interactions where orientation-dependent polarizable interactions prevail. Such interactions are highly responsive to the symmetry of the excitation cone induced by the polarizer and thus provide insight into the crystal chirality.

After proving the chiral preference of our crystals, we used chiral adsorption methods to check their stereoselectivity and chiral discrimination.

Chiral selectivity measurements

The adsorption of chiral molecules onto chiral surfaces is a standard way of measuring chirality in solids. Here, we measured the chiral induction in L-Arg-induced KIO_3 and L/D-Ala-induced $LiIO_3$ using CD and polarimetry. In the CD adsorption experiment, a 2.5 mM solution of pure L/D-TA was adsorbed at RT onto different powder concentrations. Fig. 6I presents the CD adsorption at 32 mg mL^{-1}. The control group which contains the KIO_3 without a chiral inducer showed adsorption of ~5% for both L- and D-TA without any selectivity at all (green and cyan curves, respectively). However, the addition of L-Arg to the KIO_3 crystals led to adsorption of 7% for L-TA (red curve) compared to pure L-TA (black curve) and better adsorption of (18%) onto D-TA (pink curve) compared to pure D-TA (blue curve). Fig. 6II shows the selectivity of both enantiomers to L-Arg-induced KIO_3; we see better selectivity at all concentrations to D-TA (up to 11%). Moreover, the difference between the enantiomers increases with increasing concentrations of L-Arg-induced KIO_3 crystals.

Fig. 7I illustrates the CD adsorption at a concentration of 32 mg mL^{-1}. Like KIO_3, the control group of un-induced $LiIO_3$ doesn't display discernible selectivity with an adsorption of about 20% for both L- and D-TA (orange and purple curves, respectively). L-Ala-induced $LiIO_3$ demonstrates enhanced adsorption for L-TA (48%, red curve) compared to pure L-TA (black), while D-TA exhibits 38% absorption (cyan). Superior selectivity is seen at all concentrations, which increases with the

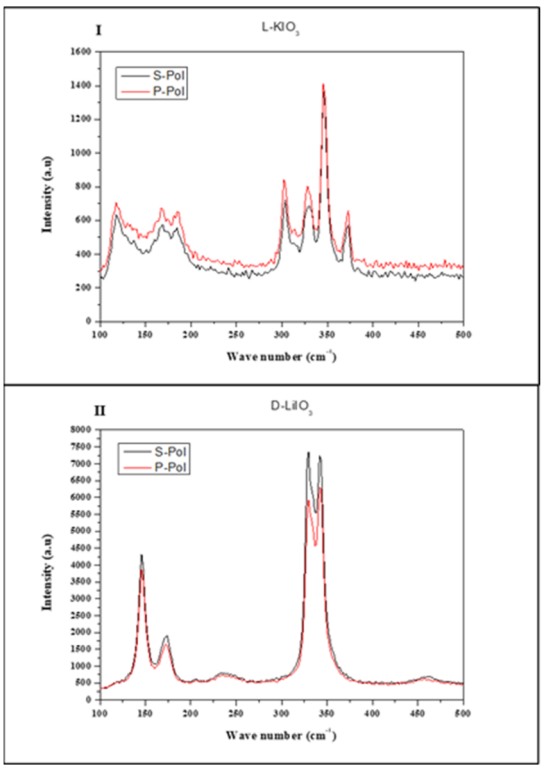

Fig. 5 LFR spectra of L-Arg-induced KIO_3 (I) and D-Ala-induced $LiIO_3$ (II). Black/red curves show signals excited using S/P-Pol.

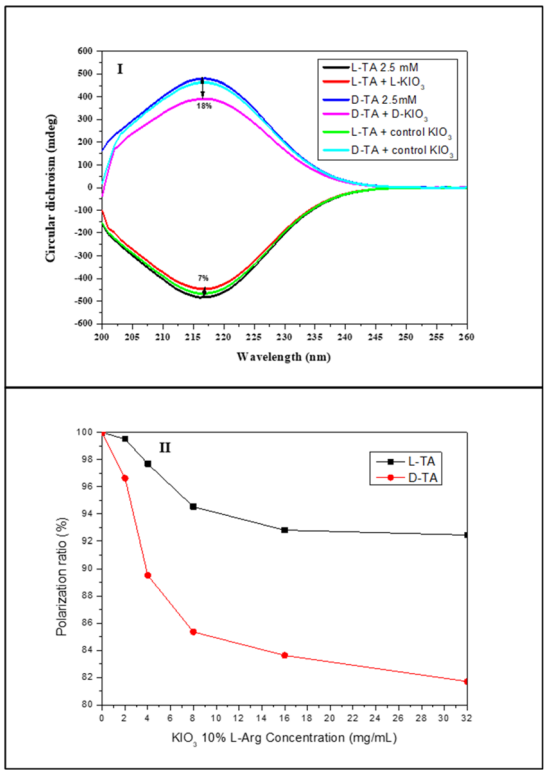

Fig. 6 Selective chiral adsorption of TA on chiral L-Arg-induced KIO_3 crystals: CD spectra of L/D-TA adsorbed onto L-Arg-induced KIO_3 (I) and selectivity of L/D-TA at different concentrations (II).

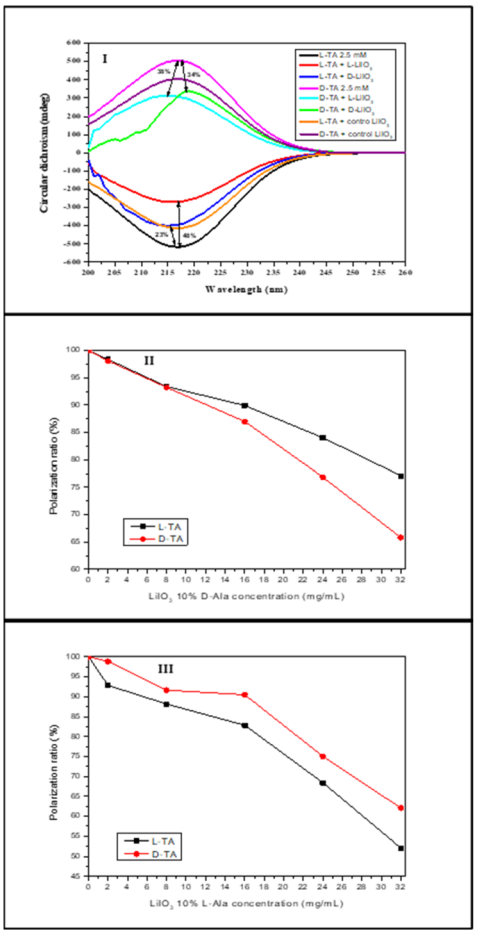

Fig. 7 Selective chiral adsorption of TA on chiral-induced $LiIO_3$ crystals – CD spectra of L/D-TA adsorbed onto L/D-Ala-induced $LiIO_3$ (I) and selectivity at different D/L-Ala-induced $LiIO_3$ concentrations (II/III).

crystal concentration up to 10% (Fig. 7III). D-Ala-induced $LiIO_3$ on the other hand shows better adsorption for D-TA (34%, green curve) compared to pure D-TA (pink), while L-TA exhibits 23% absorption onto D-Ala-induced $LiIO_3$ (blue). D-Ala-induced $LiIO_3$ crystals show better selectivity for D-TA at all concentrations, with quite similar values up to 11% (Fig. 7II).

To verify that the results obtained indeed show selectivity of the crystals, two additional measurements were made: measuring the mass change of the TA enantiomer that did not adsorb onto the crystals after evaporation of the solvent, and measuring the circular dichroism of the racemic solution of TA in order to identify any chiral sign which points to selectivity of the crystals.

Table 1 shows the results for the mass changes of the TA enantiomer that did not adsorb onto the D-Ala-induced $LiIO_3$ crystals after filtration of the crystals and evaporation of the solvent. We can see that the D-TA mass decreased more (25%) than the L-TA mass (15%) which means that the D-Ala-induced $LiIO_3$ crystals are selective in favor of D-TA. Moreover, we notice that the selective percentages are similar to the selectivity we obtained from the CD measurements (11% and 10% respectively).

Table 1 Selective chiral adsorption of TA onto D-Ala-induced $LiIO_3$ crystals by measuring the TA mass changes after crystal filtration and solvent evaporation

Crystal	D-Ala-$LiIO_3$	
Tested enantiomer	L-TA	D-TA
Vial mass (mg)	17 683.5	17 753.1
Total mass (mg)	17 693.7	17 762.1
Unadsorbed TA mass (mg)	10.2	9
Decrease from total mass (%)	15	25
Selectivity (%)	10 in favor of D-TA	

Fig. 8 presents the circular dichroism measurement of the racemic solution of TA that did not adsorb onto the D-Ala-induced $LiIO_3$ crystals. The measurement shows negative signals of the solution that indicate higher presence for the L-TA enantiomer which means that the D-Ala-induced $LiIO_3$ crystals are chiral selective in favor of D-TA.

We also examined the selective chiral adsorption on the crystal surfaces by using a polarimeter. The polarimeter adsorption experiment included pure L/D-TA 5 wt% solution that adsorbed onto L-Arg-induced KIO_3 crystal powder concentrations (2, 4, and 8 mg mL^{-1}) at RT. Fig. 9 presents the selectivity of both TA enantiomers to the L-Arg-induced KIO_3 crystals, and like the CD measurements, we can see better selectivity for the D-TA enantiomer for all concentrations. The L-Arg-induced KIO_3 shows a maximum adsorption of 7% for L-TA at the most concentrated KIO_3 compared to D-TA at the same crystal concentration with a maximum adsorption of 24%, therefore, the maximum selectivity we got was 17%. Moreover, we saw by polarimeter that the selectivity improvement as function of L-Arg-induced KIO_3 crystals' concentration increase. From the results obtained it can be noted that there is a difference of 6% between the maximum selectivity of L-Arg-induced KIO_3 we got from the CD measurements and that from the polarimeter. The difference can be explained by the lower sensitivity of the polarimeter which required more concentrated solutions for measurements that affect the amount of the TA adsorbed onto the L-Arg-induced KIO_3.

Chiral separation by crystallization[64–67] is a well-established method whereby a chiral substance such as a chiral resolving

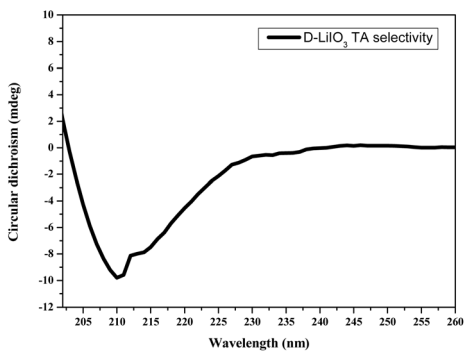

Fig. 8 Selective chiral adsorption of DL-TA on D-Ala-induced $LiIO_3$ crystals.

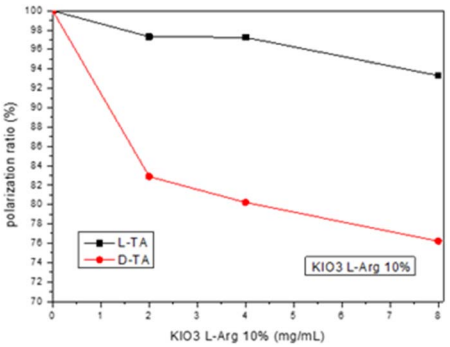

Fig. 9 Chiral selective adsorption of TA on L-Arg-induced KIO_3 crystals examined using a polarimeter.

agent or solvent is introduced in the crystallization of a racemic mixture. This method typically involves the chiral agent interacting differently with the crystals of each enantiomer during crystallization. In our case, the chiral separation is likely due to the interaction of amino acids with the ionic crystal surfaces in a chiral-specific manner. This interaction can influence the nucleation and growth processes by preferentially stabilizing one enantiomer over another. A kinetic study assessed the impact of amino acids on crystallization and chiral separation. Fig. 9 shows the results for the samples collected at various stages of crystallization.

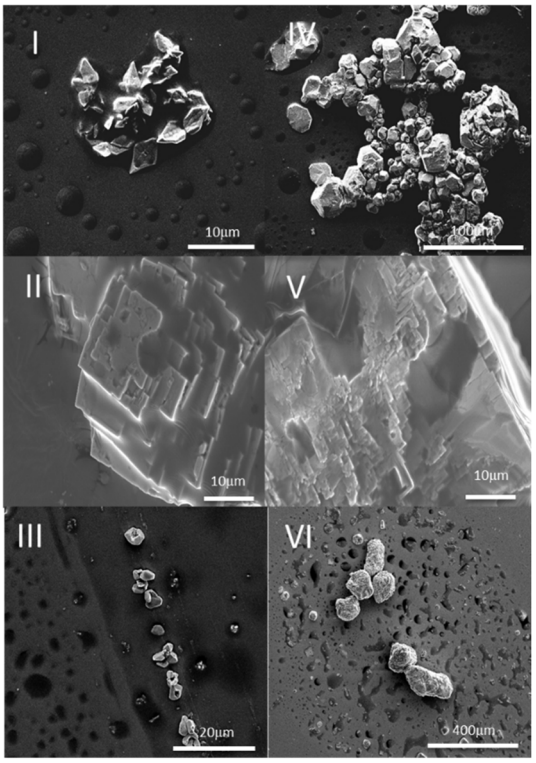

Fig. 10 HR-SEM images of kinetic crystallization of KIO_3 – control KIO_3 crystals after 4/12 h (I/IV, 10/100 μm), L-Arg-induced KIO_3 after 4/12 h (II/V, 10/10 μm) and D-Arg-induced KIO_3 after 4/12 h (III/VI, 20/400 μm).

The normal crystallization of KIO_3 after 4 h shows crystals with a uniform rhombus shape and relatively uniform size of 4.5 μm (Fig. 10I). After 12 h, crystals of various sizes were obtained resembling a dodecahedron structure with 25 μm size (Fig. 10IV). The chiral-induced crystallization presents a different phenomenon: L-Arg-induced KIO_3 shows an arrangement of square crystals on top of each other that resembles terraces (Fig. 10II and V), while D-Arg-induced KIO_3 shows such an arrangement after 12 h (Fig. 10VI) and a trapezoid structure with an average size of 4 μm after 4 h (Fig. 10III).

It should be noted that we investigated the effect of amino acid concentration on both the crystallization process and chiral induction in the crystals. A series of crystallization experiments were conducted at varying amino acid concentrations, ranging from 1% to 10% by weight relative to the crystal-forming ions. It was found that at concentrations below 10%, no chiral induction was observed. However, starting at 10% (w/w) and above, chiral induction effects were detected and maintained. At higher amino acid concentrations, no further enhancement in chiral induction was observed.

Our results suggest that amino acids can promote the formation of mesocrystals[68,69] by facilitating the organization of nanocrystals into ordered aggregates. Mesocrystals are crystalline materials consisting of nanometer-sized building blocks often referred to as "nanocrystals" arranged in a regular, repeating pattern. Unlike traditional crystals, composed of a continuous lattice of atoms or molecules, mesocrystals are made up of smaller, ordered nanocrystals that can be connected in various ways. Overall, it appears that during nucleation, amino acids preferentially bind to one chiral face of the crystal, influencing the nucleation rate, resulting in the observed chiral separation.

Conclusions

Chiral induction of the naturally occurring chiral iodate salt minerals KIO_3 and $LiIO_3$ was achieved using chiral alanine and arginine. The resultant crystals varied in morphology, size and surface roughness in contrast to the uniform crystallization obtained without chiral induction. The most prominent change was in the KIO_3 crystals, which transformed from a square to hexagonal/deformed shape in D/L-Arg-induced KIO_3. Both chiral-induced $LiIO_3$ crystals exhibited smoother surfaces. L-Ala-induced $LiIO_3$ retained a hexagonal shape, whereas D-Ala-induced $LiIO_3$ displayed an uneven morphology.

The effect of the chiral induction on KIO_3 kinetics was investigated by crystallization at different times. The presence of the chiral inducing molecules was found to affect the arrangement of the KIO_3 crystals by creating mesocrystals with a terrace arrangement.

The chiral preference of our crystals was confirmed by various direct measurements including CD of crystal pellets and LFR powder spectroscopy. Significantly, both methods were found to be applicable for direct measurement of the crystal chirality.

The enantioselectivity was also assessed by chiral adsorption measurements on the crystal surface using CD spectroscopy

and polarimetry. While L-Arg-induced KIO_3 crystals showed higher selectivity for D-TA, L-Ala-induced $LiIO_3$ showed higher selectivity for L-TA. These findings indicate that L/D-induced crystals do not necessarily improve selectivity for L/D-enantiomers; better improvement may be obtained for the other enantiomers. It should be noted that while our study primarily focuses on chiral induction, we recognize that the reversibility of this process is a crucial factor in understanding the underlying mechanisms. Many chiral crystallization studies have shown that chiral induction using chiral molecules can, in some cases, be reversible under specific conditions, such as changes in pH, temperature, or solvent environment. However, in our experiments, once chirality was induced in the crystallized products, no spontaneous reversal was observed under the experimental conditions used.

Overall, this study provides insight into the chirality of iodate salt crystals within their chiral space group. Study of the chirality and chiral discrimination of naturally occurring chiral minerals such as KIO_3 and $LiIO_3$ is important for understanding the origin of biochemical homochirality and life. Integration of chiral amino acids in the crystallization of naturally occurring chiral minerals is anticipated to provide deeper insight and a more nuanced understanding of the intricate interactions between chiral molecules and crystal surfaces. This approach holds promise for elucidating mechanisms underlying chiral discrimination in inorganic crystals as a holistic process. Utilizing chiral recognition on inorganic surfaces offers advantages across various applications, from asymmetric autocatalysis to chiral sensing and optical functionalities.

Data availability

The data that support the findings of this study are available from the corresponding author upon reasonable request. Experimental data, including raw spectra and additional supplementary information, are included in the manuscript and its ESI.† Data not included in the manuscript are available upon request, and all relevant materials will be made accessible to qualified researchers for non-commercial purposes.

Conflicts of interest

There are no conflicts to declare.

Acknowledgements

MO acknowledges the Institute for Nanotechnology and Advanced Materials at Bar-Ilan University for his Bar-Ilan President's PhD Scholarship.

Notes and references

1 D. Aquilano, F. Otálora, L. Pastero and J. M. García-Ruiz, *Prog. Cryst. Growth Charact. Mater.*, 2016, **62**(2), 227–251.
2 W. Xu, M. Cheng, S. Zhang, Q. Wu, Z. Liu, M. K. Dhinakaran, F. Liang, E. G. Kovaleva and H. Li, *Chem. Commun.*, 2021, **57**(61), 7480–7492.
3 N. Nandi and D. Vollhardt, *Curr. Opin. Colloid Interface Sci.*, 2008, **13**(1–2), 40–46.
4 D. S. Sholl, A. Asthagiri and T. D. Power, *J. Phys. Chem. B*, 2001, **105**(21), 4771–4782.
5 J. I. Putman and D. W. Armstrong, *Chirality*, 2022, **34**(10), 1338–1354.
6 J. D. Horvath and A. J. Gellman, *J. Am. Chem. Soc.*, 2002, **124**(10), 2384–2392.
7 C. E. Song and S. G. Lee, *Chem. Rev.*, 2002, **102**(10), 3495–3524.
8 A. Matsumoto, Y. Kaimori, M. Uchida, H. Omori, T. Kawasaki and K. Soai, *Angew. Chem., Int. Ed.*, 2017, **56**(2), 545–548.
9 T. Cao, Y. Li, L. Tian, H. Liang and K. Qin, *ACS Appl. Nano Mater.*, 2018, **1**(2), 759–767.
10 D. B. Amabilino, *Chem. Soc. Rev.*, 2009, **38**, 669–670.
11 D. S. Bag, T. C. Shami and K. U. B. Rao, *Sci. J.*, 2008, **58**, 626–635.
12 J. Zhang, M. T. Albelda, Y. Liu and J. W. Canary, *Chirality*, 2005, **17**, 404–418.
13 B. L. Feringa, N. P. M. Huck and A. M. Schoevaars, *Adv. Mater.*, 1996, **8**, 681–684.
14 B. L. Feringa, R. A. van Delden, N. Koumura and E. M. Geertsema, *Chem. Rev.*, 2000, **100**, 1789–1816.
15 B. L. Feringa, *Acc. Chem. Res.*, 2001, **34**, 504–513.
16 X. Y. Zhao, S. S. Perry, J. D. Horvath and A. J. Gellman, *Surf. Sci.*, 2004, **563**, 217–224.
17 C. F. McFadden, P. S. Cremer and A. J. Gellman, *Langmuir*, 1996, **12**, 2483–2487.
18 K. H. Ernst, *Curr. Opin. Colloid Interface Sci.*, 2008, **13**, 54–59.
19 A. J. Gellman, *ACS Nano*, 2010, **4**, 5–10.
20 A. Kuhnle, T. R. Linderoth and F. Besenbacher, *Top. Catal.*, 2011, **54**, 1384–1391.
21 S. M. Barlow and R. Raval, *Surf. Sci. Rep.*, 2003, **50**, 201–341.
22 Y. Mastai, *Chem. Soc. Rev.*, 2009, **38**, 772–780.
23 L. Thomsen, A. Tadich, D. P. Riley, B. C. C. Cowie and M. J. Gladys, *J. Phys. Chem. C*, 2012, **116**, 9472–9480.
24 R. Oda, F. Artzner, M. Laguerre and I. Huc, *J. Am. Chem. Soc.*, 2008, **130**, 14705–14712.
25 A. E. Baber, A. J. Gellman, D. S. Sholl and E. C. H. Sykes, *J. Phys. Chem. C*, 2008, **112**, 11086–11089.
26 C. Roth and K. H. Ernst, *Top. Catal.*, 2011, **54**, 1378–1383.
27 G. Shemer, O. Krichevski, G. Markovich, T. Molotsky, I. Lubitz and A. B. Kotlyar, *J. Am. Chem. Soc.*, 2006, **128**, 11006–11007.
28 C. Gautier and T. Burgi, *J. Am. Chem. Soc.*, 2006, **128**, 11079–11087.
29 C. Gautier and T. Burgi, *J. Am. Chem. Soc.*, 2008, **130**, 7077–7084.
30 O. Álvarez-Bermúdez, K. Landfester, K. A. I. Zhang and R. Muñoz-Espí, *Macromol. Rapid Commun.*, 2024, **45**, 2400615.
31 L. C. Preiss, M. Wagner, Y. Mastai, K. Landfester and R. Muñoz-Espí, *Macromol. Rapid Commun.*, 2016, **37**, 1421–1426.
32 L. C. Preiss, L. Werber, V. Fischer, S. Hanif, K. Landfester, Y. Mastai and R. Muñoz-Espí, *Adv. Mater.*, 2015, **27**, 2728–2732.

33 P. Paik, Y. Mastai, I. Kityk, P. Rakus and A. Gedanken, *J. Solid State Chem.*, 2012, **192**, 127–131.
34 R. Oda, I. Hue, M. C. D. J. Schmutz, S. J. Candau and F. C. MacKintosh, *Nature*, 1999, **399**, 566–569.
35 K. Sugiyasu, S. I. Tamaru, M. Takeuchi, D. Berthier, I. Hue, R. Oda and S. Shinkai, *Chem. Commun.*, 2002, **11**, 1212–1213.
36 F. Freire, J. M. Seco, E. Quiñoá and R. Riguera, *Angew. Chem., Int. Ed.*, 2011, **50**, 11692–11696.
37 F. Freire, J. M. Seco, E. Quiñoá and R. Riguera, *J. Am. Chem. Soc.*, 2012, **134**, 19374–19383.
38 M. Lui, L. Zhang and T. Wang, *Chem. Rev.*, 2015, **115**, 7304–7397.
39 L. Zhang, T. Wang, Z. Shen and M. Liu, *Adv. Mater.*, 2016, **28**, 1044–1059.
40 T. Cao, L. Mao, Y. Qiu, L. Lu, A. Banas, K. Banas, R. E. Simpson and H. C. Chui, *Adv. Opt. Mater.*, 2019, **7**(3), 1801172.
41 J. Morales-Vidal, N. R. López and M. A. Ortuño, *J. Phys. Chem. C*, 2019, **123**(22), 13758–13764.
42 Ž. Šljivančanin, K. V. Gothelf and B. Hammer, *J. Am. Chem. Soc.*, 2002, **124**(49), 14789–14794.
43 A. Ben-Moshe, S. G. Wolf, M. B. Sadan, L. Houben, Z. Fan, A. O. Govorov and G. Markovich, *Nat. Commun.*, 2014, **5**(1), 1–9.
44 R. M. Hazen and D. A. Sverjensky, *Cold Spring Harbor Perspect. Biol.*, 2010, **2**(5), a002162.
45 W. Jiang, M. S. Pacella, D. Athanasiadou, V. Nelea, H. Vali, R. M. Hazen, J. J. Gray and M. D. McKee, *Nat. Commun.*, 2017, **8**(1), 1–13.
46 R. M. Hazen and D. S. Sholl, *Nat. Mater.*, 2003, **2**(6), 367–374.
47 Y. Tanaka, T. Takeuchi, S. W. Lovesey, K. S. Knight, A. Chainani, Y. Takata, M. Oura, Y. Senba, H. Ohashi and S. Shin, *Phys. Rev. Lett.*, 2008, **100**(14), 145502.
48 G. Otis, M. Nassir, M. Zutta, A. Saady, S. Ruthstein and Y. Mastai, *Angew. Chem.*, 2020, **132**(47), 21110–21115.
49 P. Cintas, *Angew. Chem., Int. Ed.*, 2002, **41**(7), 1139–1145.
50 A. Ben-Moshe, S. G. Wolf, M. B. Sadan, L. Houben, Z. Fan, A. O. Govorov and G. Markovich, *Nat. Commun.*, 2014, **5**(1), 1–9.
51 R. M. Hazen, T. R. Filley and G. A. Goodfriend, *Proc. Natl. Acad. Sci. U. S. A.*, 2001, **98**(10), 5487–5490.
52 J. Jumas, A. Goiffon, B. Capelle, A. Zarka, J. Doukhan, J. Schwartzel, J. Detaint and E. Philippot, *J. Cryst. Growth*, 1987, **80**(1), 133–148.
53 Y. Muraoka and K. Kihara, *Phys. Chem. Miner.*, 1997, **24**(4), 243–253.
54 P. Prado-Herrero, J. Garcia-Guinea, E. Crespo-Feo and V. Correcher, *Phase Transitions*, 2010, **83**(6), 440–449.
55 L. Bayarjargal, L. Wiehl, A. Friedrich, *et al*, *J. Phys.: Condens. Matter*, 2012, **24**(32), 1–11.
56 H. Kasatani, S. Aoyagi, Y. Kuroiwa, K. Yagi, R. Katayama and H. Terauchi, *Nucl. Instrum. Methods Phys. Res., Sect. B*, 2003, **199**, 49–53.
57 L. Liu, R. Q. Wu, Z. H. Ni, Z. X. Shen and Y. P. Feng, *J. Phys.: Conf. Ser.*, 2006, **28**(1), 105–109.
58 R. Ashok Kumar, R. Ezhil Vizhi, N. Vijayan and D. Rajan Babu, *Sch. Res. Lib.*, 2011, **2**(4), 373–383.
59 A. Silambarasan, P. Rajesh, P. Ramasamy, *et al*, *Bull. Mater. Sci.*, 2017, **40**(4), 783–789.
60 V. Damle, H. Aviv and Y. R. Tischler, *Anal. Chem.*, 2022, **94**, 3188–3193.
61 H. Aviv, I. Nematsov, Y. Mastai and Y. R. Tischler, *J. Phys. Chem. A*, 2017, **121**(41), 7882–7888.
62 I. Nematsov, Y. Mastai, Y. R. Tischler and H. Aviv, *ChemPhysChem*, 2018, **19**(22), 3116–3121.
63 I. Nematsov, H. Aviv, Y. Mastai and Y. R. Tischler, *Crystals*, 2019, **9**(8), 425.
64 I. Weissbuch, L. Addadi, M. Lahav and L. Leiserowitz, *Science*, 1991, **253**(5020), 637–645.
65 G. Coquerel, *Novel Optical Resolution Technologies*, 2007, vol. 269, pp. 1–51.
66 H. Lorenz and A. Seidel-Morgenstern, *Angew. Chem.*, 2014, **53**(5), 1218–1250.
67 H. Cölfen and M. Antonietti, *Angew. Chem.*, 2005, **44**(35), 5576–5591.
68 M. Niederberger and H. Coelfen, *Phys. Chem. Chem. Phys.*, 2006, **8**(28), 3271–3287.
69 X. Xia, J. Tu, Y. Zhang, X. Wang, C. Gu, X. Zhao and H. J. Fan, *ACS Nano*, 2012, **6**(6), 5531–5538.